

Transport in armchair graphene nanoribbons and in ordinary waveguides

M. Zubair,^{1,*} M. Bahrami,^{2,†} and P. Vasilopoulos^{1,‡}

¹*Department of Physics, Concordia University, 7141 Sherbrooke Ouest, Montreal, Quebec H4B 1R6, Canada*

²*Department of Computer Science and Mathematics Nipissing University 100 College Drive, North Bay, ON, P1B 8L7, Canada*

We study dc and ac transport along armchair graphene nanoribbons using the $\mathbf{k} \cdot \mathbf{p}$ spectrum and eigenfunctions and general linear-response expressions for the conductivities. Then we contrast the results with those for transport along ordinary waveguides. In all cases we assess the influence of elastic scattering by impurities, describe it quantitatively with a Drude-type contribution to the current previously not reported, and evaluate the corresponding relaxation time for long- and short-range impurity potentials. We show that this contribution dominates the response at very low frequencies. In both cases the conductivities increase with the electron density and show cusps when new subbands start being occupied. As functions of the frequency the conductivities in armchair graphene nanoribbons exhibit a much richer peak structure than in ordinary waveguides: in the former intraband and interband transitions are allowed whereas in the latter only the intraband ones occur. This difference can be traced to that between the corresponding spectra and eigenfunctions.

I. INTRODUCTION

Graphene nanoribbons have been studied extensively theoretically and experimentally. Previous studies focused on their electronic structure, spectrum, and eigenfunctions [1], optical properties [2, 3], elementary excitations [4], magnetic susceptibility [5, 6], excitonic effects [7]. A short review of transport properties, focused on localization concepts, appeared in Ref. [8], some numerical results in Ref. [9], numerically studied thermal transport in Ref. [10], and spin transport in substitutionally doped, zig-zag graphene nanoribbons in Ref. [11]. Experimental results have also been reported [12]. The influence of impurity scattering or disorder though has received a limited attention [11]. In particular, we are not aware of any study of dc and ac transport, say, within linear-response theory, that takes into account scattering by randomly distributed impurities, most of the studies use scattering-independent Kubo formulas or consider scattering numerically.

In this work we study dc and ac transport along armchair graphene nanoribbons (AGNRs) or ordinary waveguides using linear-response, scattering-dependent and scattering-independent expressions for the conductivities. In the former case we evaluate the relaxation time for long- and short-range impurity potentials. We present the basics in Sec. II and the conductivities in Sec. III. A summary follows in Sec. IV.

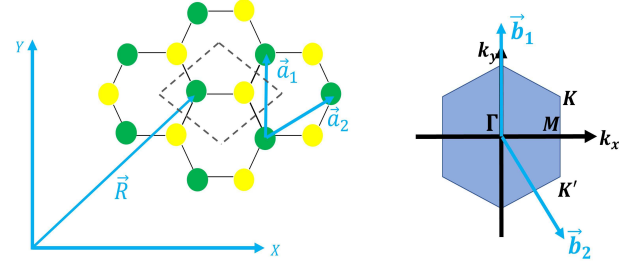


FIG. 1. Left panel: Graphene unit cell (dashed rhombus) and its primitive vectors \vec{a}_1 and \vec{a}_2 . Right panel: The corresponding Brillouin zone with \vec{b}_1 and \vec{b}_2 the reciprocal lattice vectors.

II. AGNRs, ORDINARY WAVEGUIDES

A. AGNRs

Graphene is a two-dimensional, one-atom thick planar sheet of bonded carbon atoms densely packed in a honeycomb structure as shown in the left panel of Fig. 1. In it the ribbon extends along the x axis while the graphene sheet is confined along the y axis. The lattice structure can be viewed as a triangular lattice with two sites A (green filled circles) and B (yellow filled circles) per unit cell as shown by the rectangular box in the left panel of Fig. 1. The arrows indicate the primitive lattice vectors $\vec{a}_1 = a(0, 1)$ and $\vec{a}_2 = a(1/2, \sqrt{3}/2)$, with a the triangular lattice constant of the structure, and span the graphene lattice. Further, \vec{a}_1 and \vec{a}_2 generate the reciprocal lattice vectors of the Brillouin zone, cf. Fig. 1, given by $\vec{b}_2 = 4\pi/\sqrt{3}a(\sqrt{3}/2, -1/2)$ and $\vec{b}_1 = 4\pi/\sqrt{3}a(0, 1)$. From the explicit expressions of \vec{b}_1 and \vec{b}_2 we find the two inequivalent Dirac points (valleys) given by $\vec{K} = 4\pi/3a(0, 1)$ and $\vec{K}' = 4\pi/3a(0, -1)$. The

* muhammad.zubair@mail.concordia.ca

† mousabahrami@gmail.com

‡ p.vasilopoulos@concordia.ca

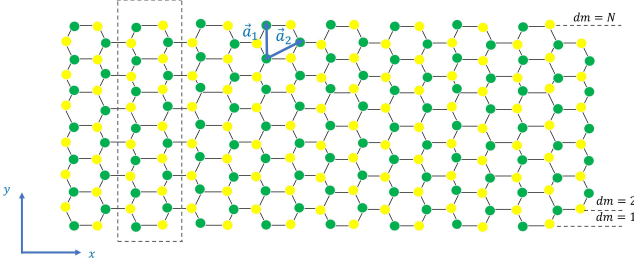


FIG. 2. Geometry of an AGNR. The dashed box shows the unit cell and dm represents the dimmer number.

$\mathbf{k} \cdot \mathbf{p}$ Hamiltonian near the Dirac points reads

$$H = \hbar v_F \begin{pmatrix} 0 & k_- & 0 & 0 \\ k_+ & 0 & 0 & 0 \\ 0 & 0 & 0 & k_+ \\ 0 & 0 & k_- & 0 \end{pmatrix}, \quad (1)$$

where \hbar is Plank's constant, v_F the Fermi velocity, and $k_{\pm} = k_y \pm ik_x$. The resulting eigenfunctions of Eq. (1) for AGNRs, shown in Fig. 2, take the form

$$\psi_{n,\eta,k_x} = \frac{1}{2\sqrt{LW}} \begin{pmatrix} \eta e^{-i\theta_{k_{yn},k_x}} e^{ik_{yn}y} \\ e^{ik_{yn}y} \\ -\eta e^{-i\theta_{k_{yn},k_x}} e^{-ik_{yn}y} \\ e^{-ik_{yn}y} \end{pmatrix} e^{ik_x x}, \quad (2)$$

where $\theta_{k_{yn},k_x} = \tan^{-1}(k_x/k_{yn})$. The energy dispersion of graphene AGNRs corresponding to Eq. (1) is [1]

$$E_{n,k_x}^{\eta} = \eta \hbar v_F \varepsilon, \quad \varepsilon = [k_{yn}^2 + k_x^2]^{1/2}, \quad (3)$$

where $\eta = +1(-1)$ stands for the conduction (valence) band. The allowed values of k_{yn} are [1, 2, 4, 5]

$$k_{yn} = \frac{n\pi}{W} - \frac{4\pi}{3a} = \frac{2\pi(3n - 2(dm + 1))}{3a(dm + 1)}; \quad (4)$$

here $W = a(dm + 1)/2$ is the ribbon width, dm the number of rows of AGNRs, $a = \sqrt{3}a_{cc}$, $a_{cc} \approx 1.42 \text{ \AA}$ is the carbon-carbon distance, and $n = 1, 2, \dots, N$ is the subband index with N the maximum number of dimmers. It follows from Eq. (4), if $3n - 2(dm + 1) = 0$, then $k_{yn} = 0$ for particular n . So, a zero energy state appears near $k_x \rightarrow 0$ as in graphene, whereas the other states have band gap because $3n - 2(dm + 1) \neq 0$. The energy dispersions for semiconducting ($dm = 4$) and metallic ($dm = 5$) nanoribbons are shown in Fig. 3.

Velocity matrix elements. To evaluate the various conductivities we need the matrix elements of the velocity operators $v_x = \partial H / \hbar \partial k_x$ and $v_y = \partial H / \hbar \partial k_y$. With

$$v_x = v_F \begin{pmatrix} \sigma_y & 0 \\ 0 & -\sigma_y \end{pmatrix}, \quad v_y = v_F \begin{pmatrix} \sigma_x & 0 \\ 0 & \sigma_x \end{pmatrix}, \quad (5)$$

their matrix elements ($|\zeta\rangle = |n, \eta, k_x\rangle$) are

$$\langle \zeta' | v_x | \zeta \rangle = N(\eta e^{i\theta_{k_{yn},k'_x}} - \eta' e^{-i\theta_{k_{yn},k_x}}) \delta_{n,n'} \delta_{k_x,k'_x} \quad (6)$$

$$\langle \zeta | v_y | \zeta' \rangle = M(\eta' e^{i\theta_{k_{yn},k_x}} + \eta e^{-i\theta_{k'_{yn},k'_x}}) \delta_{k_x,k'_x}, \quad n \neq n', \quad (7)$$

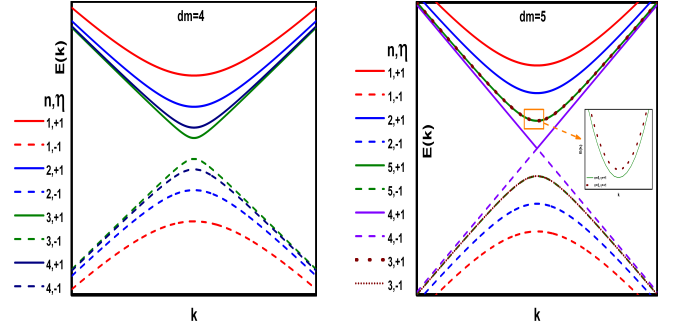


FIG. 3. Single-particle energy dispersion in AGNRs with $k = ak_x$. The left panel is for semiconducting ($dm=4$) and the right one for metallic ($dm=5$) AGNRs. The inset in the right panel shows the dispersion for $\eta = +1$ and $n=3, 5$.

with $e^{\pm i\theta_{k_{yn},k_x}} = (k_{yn} \pm ik_x)/\varepsilon_{k_x}$, $N = -iv_F/2$, and $M = -iv_F/\pi(n - n')$.

B. Ordinary waveguides

In Fig. 4 we consider an ordinary quantum wire along the x axis generated by confining a 2DEG along the y direction. We assume the confining potential $V(y)$ to be parabolic, i.e., $V(y) = m^* \omega_0^2 y^2 / 2$. The eigenvalues are

$$E_{nk_x} = (n + 1/2) \hbar \omega_0 + \hbar^2 k_x^2 / 2m^*, \quad (8)$$

and the corresponding eigenfunctions

$$\psi_{nk_x} = (2^n n! \sqrt{\pi} \ell)^{-1/2} H_n(y/\ell) e^{-y^2/2\ell^2} e^{ik_x x} \quad (9)$$

with $\ell = (\hbar/m^* \omega_0)^{1/2}$ and $H_n(y/\ell)$ the Hermite polynomials. Here only the diagonal matrix elements $v_x = \hbar k_x / m^*$ are relevant since the nondiagonal ones ($\langle \zeta' | v_x | \zeta \rangle$) vanish. However, the nondiagonal velocity matrix elements ($\langle \zeta | v_y | \zeta' \rangle$) along the confinement direction are non zero and given as

$$\langle \zeta | v_y | \zeta' \rangle = N_n [(n' + 1) \delta_{n'+1,n} - (1/2) \delta_{n'-1,n}] \delta_{k_x k'_x} \quad (10)$$

where $N_n = (i\hbar/m^* \ell) (2^n n! / 2^{n+1} n!)^{1/2}$. It is evident from the right panel of Fig. 4 that the spectrum consists of a set of equidistant, oscillator subbands due to the harmonic confinement along the y direction.

III. CONDUCTIVITIES

We consider a many-body system described by the Hamiltonian $H = H_0 + H_I - \mathbf{R} \cdot \mathbf{F}(t)$, where H_0 is the unperturbed part, H_I is a binary-type interaction (e.g., between electrons and impurities or phonons), and $-\mathbf{R} \cdot \mathbf{F}(t)$ is the interaction of the system with the external field $\mathbf{F}(t)$ [13]. For conductivity problems we have $\mathbf{F}(t) = e\mathbf{E}(t)$, where $\mathbf{E}(t)$ is the electric field, e the electron charge, $\mathbf{R} = \sum_{\mathbf{r}_i} \mathbf{r}_i$, and \mathbf{r}_i the position operator of electron i . In the representation in which H_0 is diagonal

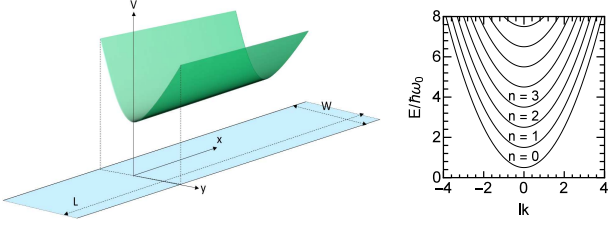


FIG. 4. Geometry of a parabolically confined (left panel), along the y direction, quantum wire of width $L_y = W$ and length $L_x = L$. The right panel shows the wire's spectrum.

the many-body density operator $\rho = \rho^d + \rho^{nd}$ has a diagonal part ρ^d and a nondiagonal part ρ^{nd} . For weak electric fields and weak scattering potentials, for which the first Born approximation applies, the conductivity tensor has a diagonal part $\sigma_{\mu\nu}^d$ and a nondiagonal part $\sigma_{\mu\nu}^{nd}$; the total conductivity is $\sigma_{\mu\nu}^T = \sigma_{\mu\nu}^d + \sigma_{\mu\nu}^{nd}$, $\mu, \nu = x, y$.

In general we have two kinds of currents, diffusive and hopping, with $\sigma_{\mu\nu}^d = \sigma_{\mu\nu}^{dif} + \sigma_{\mu\nu}^{col}$, but usually only one of them is present. If no magnetic field is present, the hopping term $\sigma_{\mu\nu}^{col}$ vanishes identically [13] and only the term $\sigma_{\mu\nu}^{dif}$ survives. For elastic scattering it is given by [13, 14]

$$\sigma_{\mu\nu}^d(\omega) = \frac{\beta e^2}{S_0} \sum_{\zeta} f_{\zeta}(1 - f_{\zeta}) \frac{v_{\nu\zeta} v_{\mu\zeta} \tau_{\zeta}}{1 + i\omega\tau_{\zeta}}, \quad (11)$$

where τ_{ζ} is the momentum relaxation time, ω the frequency, and $v_{\mu\zeta}$ the diagonal matrix elements of the velocity operator. Further, $f_{\zeta} = [1 + \exp \beta(E_{\zeta} - E_F)]^{-1}$ is the Fermi-Dirac distribution function, $\beta = 1/k_B T$, T the temperature, k_B the Boltzmann constant, and S_0 the area of the sample.

Regarding the contribution $\sigma_{\mu\nu}^{nd}$ one can use the identity $f_{\zeta}(1 - f_{\zeta'})[1 - \exp \beta(E_{\zeta} - E_{\zeta'})] = f_{\zeta} - f_{\zeta'}$ and cast the original form in the more familiar one [13, 14]

$$\sigma_{\mu\nu}^{nd}(\omega) = \frac{i\hbar e^2}{S_0} \sum_{\zeta \neq \zeta'} \frac{(f_{\zeta} - f_{\zeta'}) v_{\nu\zeta\zeta'} v_{\mu\zeta\zeta'}}{(E_{\zeta} - E_{\zeta'})(E_{\zeta} - E_{\zeta'} + \hbar\omega - i\Gamma)}, \quad (12)$$

where the sum runs over all quantum numbers $|\zeta\rangle$ and $|\zeta'\rangle$ with $\zeta \neq \zeta'$. The infinitesimal quantity ϵ in the original form [13] has been replaced by Γ_{ζ} to account for the broadening of the energy levels. In Eq. (12) $v_{\nu\zeta\zeta'}$ and $v_{\mu\zeta\zeta'}$ are the nondiagonal matrix elements of the velocity operator. Further, diagonal and nondiagonal contributions describe intraband and interband transitions, respectively, as shown schematically in Fig. 5.

A. Diagonal conductivity in ordinary waveguides

For $\omega = 0$ and $\mu = \nu = x$ Eq. (11) becomes

$$\sigma_{xx} = \frac{\beta e^2}{L} \sum_{nk_x} f_{nk_x}(1 - f_{nk_x}) v_x^2 \tau_{nk_x}. \quad (13)$$

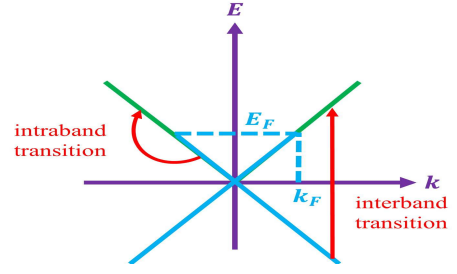


FIG. 5. Schematic representation of intraband and interband transitions in the energy dispersion of a metallic AGNR.

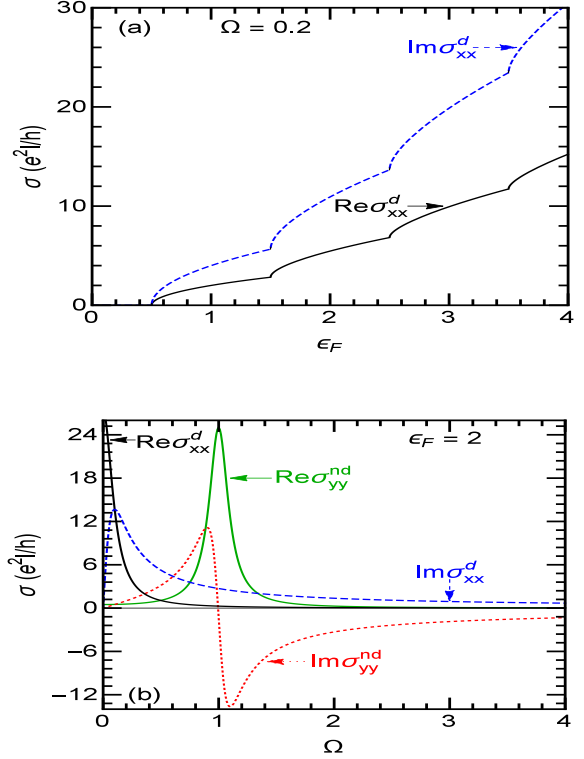


FIG. 6. Diagonal conductivity, in units of $e^2 \ell/h$ of an ordinary waveguide vs $\varepsilon_F = E_F/\hbar\omega_0$ in (a) and vs photon energy ($\Omega = \omega/\omega_0$) in (b). The black (blue) curves are for $\text{Re}\sigma_{xx}^d$ ($\text{Im}\sigma_{xx}^d$) and the dark green (red dotted) ones are for $\text{Re}\sigma_{yy}^{nd}$ ($\text{Im}\sigma_{yy}^{nd}$). Here we used $\gamma = \Gamma/\hbar\omega_0 = 0.1$.

For very low temperatures, we make the approximation $\beta f_{nk_x}(1 - f_{nk_x}) \approx \delta(E_{nk_x} - E_F)$, replace τ_{ζ} by τ_{TF} , and use the prescription $\sum_{k_x} \rightarrow (L_x/2\pi) \int dk_x$. Then Eq. (13), with $v_x = \hbar k_x/m^*$, takes the form

$$\sigma_{xx}^d(i\omega) = \frac{\sigma_0 \tau_{\text{TF}}}{(1 + i\omega\tau_{\text{TF}})} \sum_n \sqrt{E_F - E_n}, \quad (14)$$

where $E_n = (n + 1/2)\hbar\omega_0$ and $\sigma_0 = e^2/\pi\hbar\sqrt{2m^*}$. For the dc conductivity we simply set $\omega = 0$.

In Fig. 6 we show the diagonal conductivity as a function of E_F (upper panel) and photon energy (lower panel) for $\hbar\omega_0 = 0.5$ meV [15]. The conductivity increases with

the increase of E_F but cusps appear due to the presence of discrete levels in the lateral direction produced by the parabolic confinement. In addition, σ_{xx}^d vanishes when the Fermi level is in the range $0 \leq \varepsilon_F \leq 0.5$ since the electron density is null in this range of energy. We can see that $\text{Re}\sigma_{xx}^d$ has a Drude-type peak around $\Omega = 0$ while $\text{Im}\sigma_{xx}^d$ has peak around $\Omega = 0.1$ as can be seen in the lower panel of Fig. 6. Furthermore, it can also be seen that the Drude-type contribution survives at low frequencies while it vanishes at higher frequencies. Note that the nondiagonal contribution σ_{xx}^{nd} to the conductivity of 2DEG when confined in a ribbon vanishes, since the velocity matrix elements are diagonal, whereas we will find below that it survives in graphene ribbons.

B. Nondiagonal conductivity in ordinary waveguides

With the help of matrix elements (10) and $|\zeta\rangle = |n, k_x\rangle$, we can recast Eq. (12) as

$$\sigma_{yy}^{nd}(i\omega) = -\frac{ie^2}{4\pi\sqrt{2m^*}} \sum_n \int_{|E_n|}^{E_m} dE \frac{(n+1)(f_{k_x}^n - f_{k_x}^{n+1})}{[E - E_n]^{1/2}} \times \left[\frac{\hbar\omega_0 + \hbar\omega + i\Gamma}{(\hbar\omega_0 + \hbar\omega)^2 + \Gamma^2} - \frac{\hbar\omega_0 - \hbar\omega - i\Gamma}{(\hbar\omega_0 - \hbar\omega)^2 + \Gamma^2} \right] \quad (15)$$

where $E_m = E_n + \hbar^2 k_m^2 / 2m^*$. In the limit $\Gamma = \omega = 0$, one can show that $\sigma_{yy}^{nd}(i\omega)$ vanishes.

In Fig. 6 (b), we have plotted the numerically evaluated $\text{Re}\sigma_{yy}^{nd}$ (dark green curve) and $\text{Im}\sigma_{yy}^{nd}$ (red dotted curve) as functions of the dimensionless photon energy ($\Omega = \omega/\omega_0$). We can see that $\text{Re}\sigma_{yy}^{nd}$ is finite at $\Omega = 0$, due to $\Gamma \neq 0$, and attains a maximum value at $\Omega = 1$. Upon further increasing $\Omega (\geq 1)$ we see that $\text{Re}\sigma_{yy}^{nd}$ approaches to zero. On the other hand, we observe that $\text{Im}\sigma_{yy}^{nd}$ acquires positive and negative values due to the $\hbar\omega_0 - \hbar\omega$ factor in Eq. (15). For $\hbar\omega_0 > \hbar\omega$, the second term of Eq. (15) is greater than the first one and we find the positive peak. However, we obtain a negative absorption peak for $\hbar\omega_0 < \hbar\omega$. It can also be seen from Eq. (15) that only intraband transitions occur in contrast to AGNRs where both intraband and interband transitions occur, see Eqs. (28)-(29) below.

C. Diagonal conductivity in AGNRs

τ constant. From Eq. (3) we readily find the velocity

$$v_x = \eta v_F k_x / \varepsilon. \quad (16)$$

Substituting Eq. (16) in Eq. (11), using $\beta f_{\eta k_x}^n (1 - f_{\eta k_x}^n) \approx \delta(E_{\eta k_x}^n - E_F)$ and $\tau_{\eta k_x}^n = \tau_F$ at zero temperature, and performing the integration over $k_x ((L_x/2\pi) \int dk_x)$, we find the conductivity expression of AGNRs for finite ω as

$$\sigma_{xx}^d(i\omega) = \frac{e^2 v_F \tau_F}{h(1 + i\omega\tau_F)} \sum_n \frac{X_{Fn}}{\varepsilon_F}, \quad (17)$$

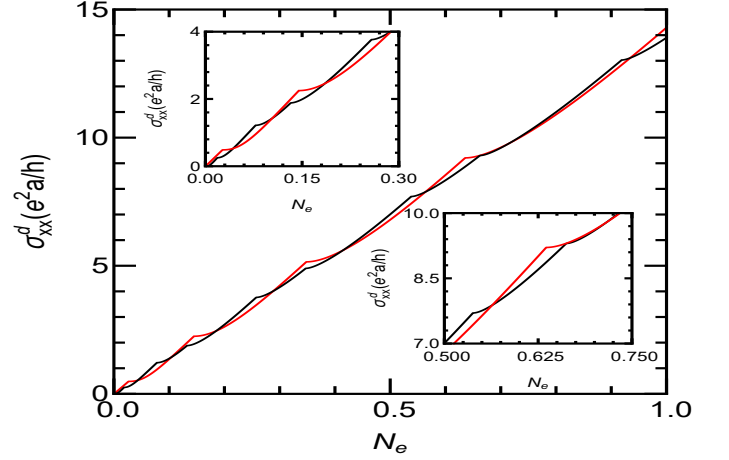


FIG. 7. Conductivity σ_{xx}^d for screened Coulomb scatterers as a function of the dimensionless carrier density ($N_e = an_e/2\pi$) for semiconducting (black curves) and metallic (red curves) nanoribbons. Cusps in the curves appear when new subbands are occupied by increasing the electron density. For further clarity the ranges 0–0.3 and 0.5–0.75 are shown in the insets.

where $X_{Fn} = [\varepsilon_F^2 - k_{yn}^2]^{1/2}$, $\varepsilon_F = E_F/\hbar v_F$, and the summation terminates at the last occupied level. Equation (17) is only valid for $\varepsilon_F \geq k_{yn}$. For $k_{yn} = 0$ it reduces to

$$\sigma_{xx}^d(i\omega) = \frac{e^2 v_F \tau_F}{h(1 + i\omega\tau_F)} n_F, \quad (18)$$

where n_F is the number of occupied levels. $\tau \neq$ **constant**. *Long-range impurities*. Using Eqs. (16), (A4), and the same assumptions, as given above Eq. (17), in Eq. (11) we obtain for $\omega = 0$ and $\eta = +1$

$$\sigma_{xx}^d(0) = \frac{e^2 A}{h} \sum_n \frac{X_{Fn}^2}{\varepsilon_F^2} \left[\frac{k_s^2 + 4X_{Fn}^2}{k_s + [k_s^2 + 4X_{Fn}^2]^{1/2}} \right], \quad (19)$$

with $A = 2\hbar^2 v_F^2 / n_i U_s^2$. For $k_{yn} = 0$ Eq. (19) becomes

$$\sigma_{xx}^d(0) = \frac{e^2 A}{h} \frac{k_s^2 + 4\varepsilon_F^2}{k_s + [k_s^2 + 4\varepsilon_F^2]^{1/2}} n_F. \quad (20)$$

Short-range impurities. We consider the potential $U(x) = U_0 \delta(x - x_i)$ with U_0 its constant strength and x_i the position of the impurity. Corresponding to Eq. (19) we find the dc conductivity is now given by

$$\sigma_{xx}^d(0) = \frac{e^2 B}{h} \sum_n \frac{X_{Fn}^2}{\varepsilon_F^2}, \quad (21)$$

where $B = \pi \hbar^2 v_F^2 / 2n_i U_0^2$. For $k_{yn} = 0$ Eq. (21) becomes

$$\sigma_{xx}^d(0) = \frac{e^2 B}{h} n_F. \quad (22)$$

For the finite frequency ω results we simply divide those of Eqs. (19)-(22) by $1 + i\omega\tau_F$.

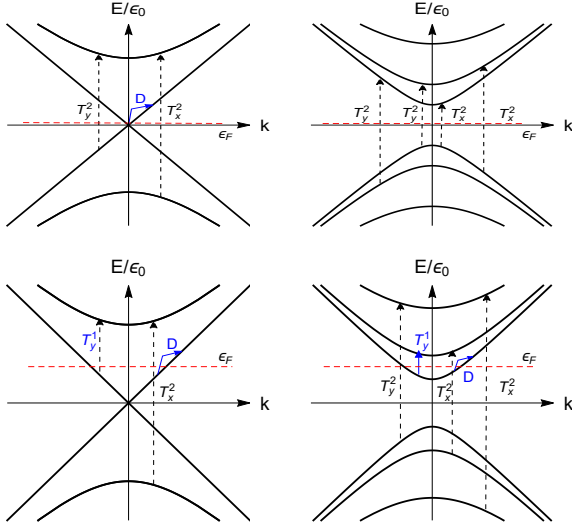


FIG. 8. Schematic representation of some allowed transitions indicated by arrows. The horizontal red dashed lines show the Fermi level. T_y^i and T_x^i denote intraband ($i = 1$) and interband ($i = 2$) transitions, respectively at the peaks of σ_{yy} and σ_{xx} in Fig. 9, see Eqs. (25)-(29), while D represents the Drude-type intraband transition, cf. Eq. (17).

In Fig. 7, we plot σ_{xx}^d as a function of the dimensionless carrier density ($N_e = an_e/2\pi$) for $dm = 4$ (black line) and $dm = 5$ (red line). The relevant relaxation time is given by Eq. (A4) in appendix. The factor k_s can be approximated by the Thomas-Fermi wave vector $k_s = (2\pi e^2/\epsilon)D(E_F)$ with ϵ the relative dielectric constant and $D(E_F)$ the density of states at the Fermi level. We can see that σ_{xx}^d increases almost linearly from 0 with the peaks at critical value of N_e . These peaks appear when the subbands start to be occupied by electrons. Also, this behaviour is consistent with the band structures, cf. Fig. 3. These jumps are absent in the conductivity of graphene [16]. Further, we observe the richer structure of peaks for semiconducting ribbons than metallic ones due to the opening of gaps among the subbands of semiconducting nanoribbons as can be seen by comparing the left and right panels of Fig. 3. It is worth mentioning that this scattering-dependent contribution was not accounted for in previous studies, see, e.g., Refs. [2], [5].

D. Nondiagonal conductivity in AGNRs

With $|\zeta\rangle = |n, \eta, k_x\rangle$ Eq. (12) becomes

$$\sigma_{xx}^{nd}(i\omega) = \frac{i\hbar e^2}{L_x} \sum_{\eta\eta'nn'k_xk'_x} \frac{f_{\eta k_x}^n - f_{\eta' k'_x}^{n'}}{E_{\eta k_x}^n - E_{\eta' k'_x}^{n'}} \times \frac{v_{x\eta\eta'k_x}^{nn'} v_{x\eta'k'_x}^{n'n}}{E_{\eta k_x}^n - E_{\eta' k'_x}^{n'} + \hbar\omega + i\Gamma_{\eta\eta'k_xk'_x}^{nn'}}, \quad (23)$$

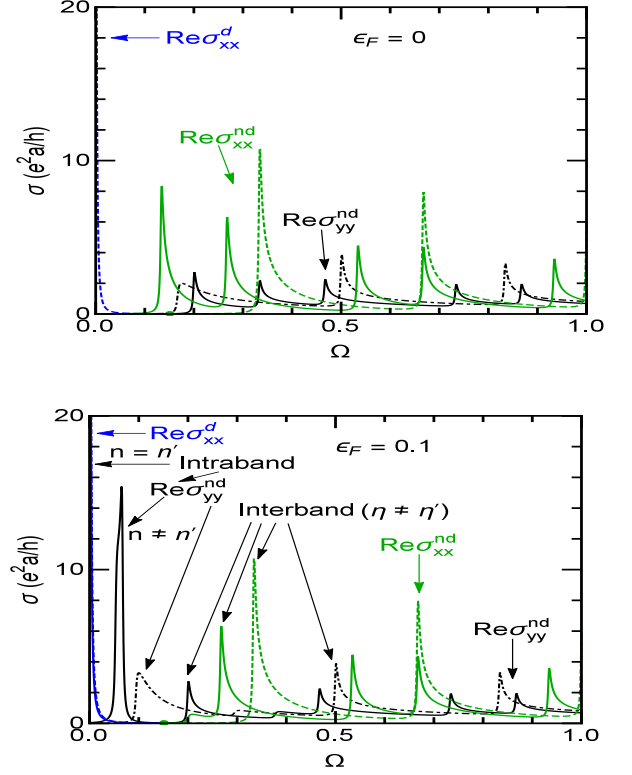


FIG. 9. Real part of the conductivity vs frequency for $\varepsilon_F = 0$ (upper panel) and $\varepsilon_F = 0.1$ (lower panel, $k_B T/\varepsilon_0 = 0.001$, and $\Gamma/\varepsilon_0 = 0.002$). The solid curves are for semiconducting nanoribbons ($dm = 4$) and the dotted ones are for metallic ribbons ($dm = 5$).

where $v_{x\eta\eta'k_x}^{nn'} = \langle n', \eta', k'_x | v_x | n, \eta, k_x \rangle$ and $v_{x\eta'k'_x}^{n'n} = \langle n', \eta', k'_x | v_x | n, \eta, k_x \rangle$ are the nondiagonal matrix elements of the velocity operator. Further, the velocity matrix element (6) is diagonal in k_x , therefore k_x will be suppressed in order to simplify the notation. The summation in Eq. (23) runs over all quantum numbers n, n', η, η' , and k_x . The parameter $\Gamma_{\eta\eta'}^{nn'}$, that takes into account the level broadening, is assumed to be independent of the band and subband indices i.e. $\Gamma_{\eta\eta'}^{nn'} = \Gamma$. Also, we will simplify the notation over summation by considering the subband orthogonality $\delta_{k_y n, k'_y n'}$. Hence, after expanding the fraction, Eq. (23) can be rewritten as

$$\sigma_{xx}^{nd}(i\omega) = \frac{i\hbar e^2}{L_x} \sum_{\eta\eta'nk_x} \frac{(f_{\eta k_x}^n - f_{\eta' k_x}^{n'}) v_{x\eta\eta'k_x}^{nn} v_{x\eta'k_x}^{nn}}{E_{\eta k_x}^n - E_{\eta' k_x}^{n'}} \times \frac{E_{\eta k_x}^n - E_{\eta' k_x}^{n'} + \hbar\omega - i\Gamma}{(E_{\eta k_x}^n - E_{\eta' k_x}^{n'} + \hbar\omega)^2 + \Gamma^2}. \quad (24)$$

We evaluate Eq. (24) by considering the summation over $\eta = +1, \eta' = -1$, and $\eta = -1, \eta' = +1$, denoted by \sum_{-+} and \sum_{+-} . For $\eta = \eta'$ the contributions \sum_{++} and \sum_{--} to $\text{Re}\sigma_{xx}^{nd}(i\omega)$ are not allowed due to the condition $\zeta \neq \zeta'$, cf. Eqs. (6), (11). Hence, the summation over

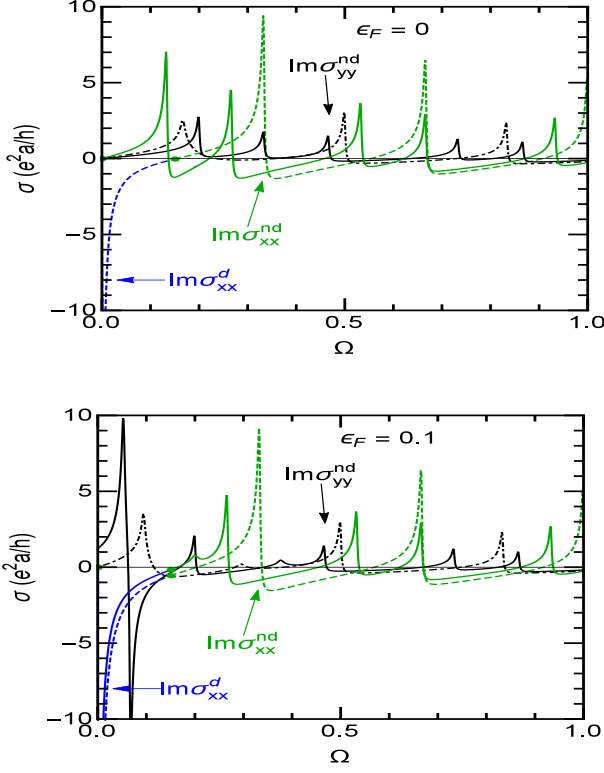


FIG. 10. As in Fig. 9 but for the imaginary part of the total conductivity vs frequency.

$\eta = \eta'$ is given only by the Drude-type, intraband contribution $\sigma_{xx}^d(i\omega)$ to the total conductivity, see Eqs. (15), (17).

The real and imaginary parts corresponding to Eq. (24) read

$$\text{Re}\sigma_{xx}^{nd}(i\omega) = -\frac{e^2 v_F}{4\pi} \sum_n \int_{|k_{yn}|}^{\varepsilon_m} d\varepsilon \frac{k_{yn}^2 (f_{-k_x}^n - f_{+k_x}^n)}{\varepsilon^2 [\varepsilon^2 - k_{yn}^2]^{1/2}} \times (C_+ + C_-), \quad (25)$$

and

$$\text{Im}\sigma_{xx}^{nd}(i\omega) = -\frac{e^2 v_F}{4\pi} \sum_n \int_{|k_{yn}|}^{\varepsilon_m} d\varepsilon \frac{k_{yn}^2 (f_{-k_x}^n - f_{+k_x}^n)}{\varepsilon^2 [\varepsilon^2 - k_{yn}^2]^{1/2}} \times (R_+ - R_-), \quad (26)$$

with $\varepsilon_m = (k_m^2 + k_{yn}^2)^{1/2}$ and k_m the maximum value of k_x below for which the $\mathbf{k} \cdot \mathbf{p}$ theory is valid. Further, $v_{x+k_x}^{nn} v_{x-k_x}^{nn} = v_{x+k_x}^{nn} v_{x-k_x}^{nn} = v_F^2 k_{yn}^2 / \varepsilon^2$ [see Eq. (6)], $C_{\pm} = \Gamma((2\hbar v_F \varepsilon \pm \hbar\omega)^2 + \Gamma^2)^{-1}$, and $R_{\pm} = (2\hbar v_F \varepsilon \pm \hbar\omega)((2\hbar v_F \varepsilon \pm \hbar\omega)^2 + \Gamma^2)^{-1}$. In the limit $k_{yn} = 0$, the real and imaginary parts of the nondiagonal conductivity will vanish as is evident from Eqs. (25)-(26). Further, for $\omega = 0$ and $\Gamma \neq 0$, the real part [see Eq. (25)] of the nondiagonal conductivity survives whereas the imaginary one vanishes [see Eq. (26)]. Also, it can be seen from Eqs. (25) and (26) that transitions occur between the valence and conduction band with the same index n .

Some of these transitions are shown schematically in Fig. 8 for two values of the Fermi level (dashed red lines) with T_y^i and T_x^i denoting the intraband ($i = 1$) and interband ($i = 2$) ones, respectively at the peaks of σ_{xx}^{nd} and σ_{yy}^{nd} .

For $T = 0$ and E_F in the gap we have $f_{-k_x}^n = 1$ and $f_{+k_x}^n = 0$. After evaluating the integrals over ε in Eqs. (25)-(26) we rewrite them in the combined form

$$\sigma_{xx}^{nd}(i\omega) = \frac{ie^2 U_+}{h(\omega_1^2 + \Gamma_1^2)} \sum_n \left[1 + \frac{2iU_+ k_{yn}^2}{(\omega_1^2 + \Gamma_1^2)p} \ln \frac{Q_+}{Q_-} \right], \quad (27)$$

where $\omega_1 = \hbar\omega/\hbar v_F$, $\Gamma_1 = \Gamma/\hbar v_F$, $U_{\pm} = (\omega_1 \pm i\Gamma_1)$, $p = (4k_{yn}^2 - U_{\pm}^2)^{1/2}$, and $Q_{\pm} = p \pm iU_{\pm}$.

For $\text{Re}\sigma_{yy}^{nd}(i\omega)$ we follow the same procedure and from the sum over $n' (\neq n)$, cf. Eq. (7), we keep only the dominant terms $n' = n \pm 1$. We then obtain

$$\text{Re}\sigma_{yy}^{nd}(i\omega) = \frac{e^2 \hbar v_F}{h\pi^2} \sum_n \int_0^{k_m} dk_x \times \left[\frac{(f_+^n - f_+^{n\pm 1})D_+ - (f_-^n - f_-^{n\pm 1})D_-}{\varepsilon_{k_x}^n - \varepsilon_{k_x}^{n\pm 1}} + \frac{(f_+^n - f_-^{n\pm 1})D_+ - (f_-^n - f_+^{n\pm 1})D_-}{\varepsilon_{k_x}^n + \varepsilon_{k_x}^{n\pm 1}} \right] \quad (28)$$

and

$$\text{Im}\sigma_{yy}^{nd}(i\omega) = \frac{e^2 \hbar v_F}{h\pi^2} \sum_n \int_0^{k_m} dk_x \times \left[\frac{(f_+^n - f_+^{n\pm 1})E_+ + (f_-^n - f_-^{n\pm 1})E_-}{\varepsilon_{k_x}^n - \varepsilon_{k_x}^{n\pm 1}} + \frac{(f_+^n - f_-^{n\pm 1})E_+ + (f_-^n - f_+^{n\pm 1})E_-}{\varepsilon_{k_x}^n + \varepsilon_{k_x}^{n\pm 1}} \right], \quad (29)$$

where $D_{\pm} = \Gamma((\hbar v_F \varepsilon_{k_x}^n - \hbar v_F \varepsilon_{k_x}^{n\pm 1} \pm \hbar\omega)^2 + \Gamma^2)^{-1}$, and $E_{\pm} = (\hbar v_F \varepsilon_{k_x}^n + \hbar v_F \varepsilon_{k_x}^{n\pm 1} \pm \hbar\omega)((\hbar v_F \varepsilon_{k_x}^n + \hbar v_F \varepsilon_{k_x}^{n\pm 1} \pm \hbar\omega)^2 + \Gamma^2)^{-1}$ with $\varepsilon_{k_x}^n = (k_{yn}^2 + k_x^2)^{1/2}$. According to Eqs. (28) and (29), the absorption occurs between the valence band with index n and the conduction band with $n \pm 1$. The integrals over k_x in Eqs. (28) and (29) are not tractable and we evaluate them numerically.

In Fig. 9 we show $\text{Re}\sigma_{xx}$ and $\text{Re}\sigma_{yy}$ as functions of Ω for $\varepsilon_F = 0$ (upper panel) and $\varepsilon_F = 0.1$ (lower panel). The solid curves are for semiconducting nanoribbons ($dm = 4$) and the dotted ones for metallic ribbons ($dm = 5$). The optical selection rules ($n - n' = \Delta n$) allow subband index n to change by only 0 along the x (wire) direction. However, we have $\Delta n = \pm 1$ along the y (confinement) direction, but the amplitude of the peaks is small. Hereafter, we call the transitions satisfying $\Delta n = 0$ direct transitions and those satisfying $\Delta n = \pm 1$ indirect transitions. In addition, one needs to go from occupied to unoccupied states through the absorption of photons. The series of peaks corresponding to $\text{Re}\sigma_{xx}$ and $\text{Re}\sigma_{yy}$ occur at $\hbar\omega = -E_{-k_x}^n + E_{+k_x}^n$ and $\hbar\omega = -E_{-k_x}^n + E_{+k_x}^{n+1}$, respectively. These peaks correspond to the allowed interband transitions in the energy

spectrum. The position of the absorption peaks follows the same order as indicated in Fig. 8. These results for AGNRs are similar to those in Ref. [5] apart from the contribution $\sigma_{\mu\mu}^d(i\omega)$ which is completely absent and only the real parts of the conductivities $\sigma_{\mu\mu}^{nd}(i\omega)$ are plotted.

In the upper panel of Fig. 9 in which Fermi level is in gap i.e., $\varepsilon_F = 0$, we can see that a Drude-type intraband transition is allowed in $\text{Re}\sigma_{xx}$ for $dm = 5$ due to the nonvanishing v_x velocity matrix elements with $\Delta n = 0$ [see Eq. (6) and transition D in Fig. 8]. On the other hand, we cannot see any type of intraband transitions in $\text{Re}\sigma_{yy}$ because v_y the velocity matrix elements vanish as can be seen from Eq. (6). However, for $dm = 4$, only interband absorption transitions are allowed due to the Pauli exclusion principle in both $\text{Re}\sigma_{xx}$ and $\text{Re}\sigma_{yy}$. But, when we move the Fermi level to 0.1 [see the red dashed curve in Fig. 8], the absorption peak, say T_x^1 , in $\text{Re}\sigma_{xx}$ is suppressed due to the Pauli exclusion principle for $dm = 4$ in the range $0.017 \leq \Omega \leq 0.27$ whereas an absorption peak due to intraband transition (T_y^1) appears in $\text{Re}\sigma_{yy}$ as can be seen in the lower panel of Fig. 9. Moreover, a Drude absorption peak appears at low Ω in $\text{Re}\sigma_{xx}$ for both $dm = 4$ and $dm = 5$. One noteworthy feature is that resonance energies $E_{+k_x}^n - E_{-k_x}^{n+1}$ of indirect transitions are appeared between the $E_{+k_x}^n - E_{-k_x}^n$ that are the energies corresponding to absorption peaks of direct transitions.

We have plotted $\text{Im}\sigma_{xx}$ and $\text{Im}\sigma_{yy}$ versus the dimensionless photon energy (Ω) in Fig. 10. The absorption peaks in $\text{Im}\sigma_{xx}$ have negative and positive values due to the negative sign between R_+ and R_- terms in Eq. (26), and the peaks corresponding to the transitions $-n \rightarrow n$ and $n \rightarrow -n$ have slightly different energies. This mismatch creates positive and negative peaks in the conductivity. However, the amplitude of the negative peaks is small as compared to that of the positive ones. This argument applies also to $\text{Im}\sigma_{yy}$ [see Eq. (29)].

IV. SUMMARY AND CONCLUSION

We studied dc and ac transport in both metallic and semiconducting AGNRs. We derived analytical expressions for the diagonal and nondiagonal conductivities by employing linear response theory. We found that semiconducting to metallic transitions occur by changing the number of rows (dm) [see Fig. 3] in contrast to ordinary waveguides in which such transitions do not occur, see Fig. 4. In addition, the diagonal conductivity for scattering by screened Coulomb impurities was shown to depend approximately linearly on the carrier density and exhibits upward cusps when the Fermi level crosses the subbands. Further, we showed that the diagonal conductivity varies approximately linearly with the electron concentration in AGNRs, cf. Fig. 7.

Importantly, in all cases we showed that the scattering-dependent conductivity is described quantitatively by a Drude-type contribution $\sigma_{xx}^d(i\omega)$ which, to our knowl-

edge, was not previously reported or explicitly evaluated. We did show that this contribution dominates the response at very low frequencies at which the usual, scattering-independent contribution near vanishes.

Moreover, we obtained the optical selection rules $\Delta n = 0$ along the wire and $\Delta n = \pm 1$ along the confinement direction of AGNRs. We have demonstrated that the peak amplitude of the indirect transitions is suppressed contrary to that of the direct ones. Also, we showed that the absorption of low-energy photons is sensitive to the variation of the Fermi level, in contrast to monolayer WSe₂ [17], in which the spectral weight of the interband peaks is continuously redistributed into the intraband ones [see Fig. 9] similar to that of other 2D materials [18] like graphene, silicene, $\alpha - T_3$, and topological insulators. A similar behaviour was found for the imaginary part of the conductivity. Furthermore, only intraband transitions occur in ordinary waveguides, cf. Fig. 6 (b) and Eq. (15), in contrast to AGNRs in which both intra- and inter-band transitions occur [see Figs. (9)-(10) and Eqs. (28)-(29)].

The details of the previous paragraphs could best be tested, we think, by optical experiments in AGNRs and by contrasting their results with those in unconfined graphene or other 2D materials and standard waveguides. The peak positions, that are sensitive to the dm -dependent energy gap between the subbands, cf. Eq. (3), could be tuned by a careful choice of dm in experiments performed in the far infrared (IR) range. This could lead to the development of new optical devices, in particular novel IR photodetectors based on photon absorption rather than on thermionic emission or tunnelling in arrays of GRNs proposed in Ref. [20]. Moreover, the scattering-dependent contribution $\sigma_{xx}^d(i\omega)$ to the power spectrum should be evident at very low frequencies at which the other conductivity contributions $\sigma_{\mu\nu}^{nd}(i\omega)$, as well as $\sigma_{yy}^d(i\omega)$ in our case, vanish ($\Gamma = 0$) or nearly so ($\Gamma \neq 0$) and $\sigma_{xx}^d(i\omega)$ dominates the spectrum, cf. Ref. [14]. We are not aware of any such experiments but hope that they will be carried out and also test the selection rules $\Delta n = 0$ and $\Delta n = \pm 1$ mentioned above.

ACKNOWLEDGMENTS

M. Z. and P. V. acknowledge the support of the Concordia University Grant No. VB0038 and Concordia University Graduate Fellowship.

Appendix A: relaxation time

Within the first Born approximation, the standard formula for relaxation time takes the form

$$\frac{1}{\tau_\zeta} = \frac{1}{\tau_{\eta k_x}^n} = \frac{2\pi n_i}{\hbar L_x} \sum_{n', \eta', k'_x} |\langle n, \eta, k_x | U_x | n', \eta', k'_x \rangle|^2 \times \delta(E_{\eta k_x}^n - E_{\eta' k'_x}^{n'}) (1 - \cos \theta), \quad (\text{A1})$$

where $U_x = U(x)$ is the impurity potential, n_i the impurity density, and θ the angle between the initial (k_{yn}, k_x) and final (k'_{yn}, k'_x) wave vectors. Equation (A1) holds only for the elastic scattering. The results for two types of impurity potentials are as follows.

Long-range impurities: For screened, Coulomb-type impurities we consider the model potential [19]

$$U_x = U_0 e^{-k_s |x|} / \sqrt{|x|}, \quad (\text{A2})$$

where $U_0 = 2\pi e^2 \sqrt{c} / \epsilon_0 \epsilon_r$, k_s is the screening wave vector, ϵ_0 the free space permittivity, ϵ_r the static dielectric constant, and c is the constant of order 1 in units of inverse length. In this case, we write $U_x = \sum_{q_x} U_{q_x} e^{iq_x x}$ with $U_{q_x} = U_0 \{ [k_s + \sqrt{k_s^2 + q_x^2}] / (k_s^2 + q_x^2) \}^{1/2}$ the Fourier transform of U_x . We obtain

$$|\langle n, \eta, k_x | e^{iq_x x} | n', \eta', k'_x \rangle|^2 = |\eta \eta' + e^{-i\varphi}|^2 |U_{q_x}|^2 \times \delta_{n, n'} \delta_{k'_x + q_x, k_x}, \quad (\text{A3})$$

with $q_x = k_x - k'_x$ and $\varphi = \theta_{k_{yn}, k_x} - \theta_{k'_{yn}, k'_x}$. The integration over q_x is straightforward. That over k'_x is carried

out using the properties of the δ function and only the root $k'_x = -k_x$ of the equation $E_{\eta k_x}^n - E_{\eta' k'_x}^{n'} = 0$ contributes to the integral. For simplicity we also take $\varphi \approx 0$ and use $\theta \approx \pi$. With k_x evaluated at the Fermi level the final result is

$$\frac{1}{\tau_F} = \frac{n_i U_0^2}{2\hbar^2 v_F} \frac{\sqrt{k_{yn}^2 + |k_F|^2} (k_s + k_{sF})}{|k_F| k_{sF}^2}, \quad (\text{A4})$$

where $k_{sF}^2 = k_s^2 + 4|k_F|^2$. The term k_{yn} in Eq. (A4) denotes the Fermi wave vector for the n th subband. In the limit $k_{yn} = 0$ Eq. (A4) becomes

$$\frac{1}{\tau_F} = \frac{n_i U_0^2}{2\hbar^2 v_F} \frac{k_s + k_{sF}}{k_{sF}^2}. \quad (\text{A5})$$

Further, for $k_s \gg k_F$, Eq. (A5) reduces to

$$\frac{1}{\tau_F} = \frac{n_i U_s^2}{\hbar^2 v_F k_s}. \quad (\text{A6})$$

Short-range impurities: we have $U(x) = U_0 \delta(x - x_i)$ with U_0 the constant strength of potential and x_i the position of the impurity. In this case, the matrix element becomes $|\langle n, \eta, k_x | U_x | n', \eta', k'_x \rangle|^2 = U_0^2$. This leads to

$$\frac{1}{\tau_F} = \frac{2n_i U_0^2}{\pi \hbar^2 v_F} \frac{\sqrt{k_{yn}^2 + |k_F|^2}}{|k_F|}. \quad (\text{A7})$$

For $k_{yn} = 0$ Eq. (A7) reduces to

$$\frac{1}{\tau_F} = \frac{2n_i U_0^2}{\pi \hbar^2 v_F}. \quad (\text{A8})$$

-
- [1] L. Brey and H. A. Fertig, Phys. Rev. B **75**, 125434 (2007); H. Zheng, Z. F. Wang, Tao Luo, Q. W. Shi, and J. Chen, *ibid.* **75**, 044710 (2011);
- [2] K.-I. Sakaki, K. Wakabayashi, and T. Enoki, J. Phys. Soc. Jpn. **80**, 044710 (2011); M.-F. Lin and F.-L. Shyu, *ibid.* **69**, 3529 (2000); K. Gundra and A. Shukla, Phys. Rev. B **83**, 075413 (2011).
- [3] Ken-ichi Sasaki, K. Kato, Y. Tokura, K. Oguri, and T. Sogawa, Phys. Rev. B **84**, 085458 (2011).
- [4] L. Brey and H. A. Fertig, Phys. Rev. B **73**, 235411 (2006); K. O. Wedel, N. A. Mortensen, K. S. Thygesen, and M. Wubs, Phys. Rev. Lett. **98**, 155412 (2018); M. Bahrami and P. Vasilopoulos, Optics Express **25**, 16840 (2017).
- [5] Y. Ominato and M. Koshino, Phys. Rev. B **85**, 165454 (2012); Solid State Commun. **175-176**, 51 (2013).
- [6] J. Liu, Z. Ma, A. R. Wright, and C. Zhang, J. Appl. Phys. **103**, 103711 (2008).
- [7] Li Yang, M. L. Cohen, and S. G. Louie, Nano Lett. **7**, 3112 (2007).
- [8] K. Wakabayashi, Y. Takane, M. Yamamoto, and M. Sigrist, New J. Phys. **11**, 095016 (2009).
- [9] Thomas Aktor, Antti-Pekka Jauho, and Stephen R. Power, Phys. Rev. B **33**, 035446 (2016); J. Guo, D. Gunlycke, and C. T. White, Appl. Phys. Lett. **92**, 163109 (2008); P. Hawkins, M. Begliarbekov, M. Zivkovic, S. Strauf, and C. P. Search, J. Phys. Chem. C **116**, 18382 (2012).
- [10] J. Lan, J.-S. Wang, C. K. Gan, and S. K. Chin, Phys. Rev. B **79**, 115401 (2009); Ming-Xing Zhai and Xue-Feng Wang, Sci. Rep. **6**, 36762 (2016).
- [11] Ting-Ting Wu, Xue-Feng Wang, Ming-Xing Zhai, Hua Liu, Liping Zhou, and Yong-Jin Jiang, Appl. Phys. Lett. **100**, 052112 (2012).
- [12] O. Grning, S. Wang, X. Yao, C. A. Pignedoli, G. B. Barin, C. Daniels, A. Cupo, V. Meunier, X. Feng, A. Narita, K. Müllen, P. Ruffieux, and R. Fasel, Nature **560**, 209 (2018); G. Z. Magda, X. Jin, I. Hagymasi, P. Vancso, Z. Osvath, P. Nemes-Incze, C. Hwang, L. P. Biro, and L. Tapaszto, Nature **514**, 608 (2014); M. Y. Han, J. C. Brant, and P. Kim, Phys. Rev. Lett. **104**, 056801 (2010).
- [13] M. Charbonneau, K. M. Van Vliet, and P. Vasilopoulos, J. Math. Phys. **23**, 318 (1982).
- [14] V. Vargiamidis, P. Vasilopoulos and G.-Q. Hai, J. Phys.: Condens. Matter **26**, 345303 (2014); V. Vargiamidis, and P. Vasilopoulos, J. Appl. Phys. **116**, 063713 (2014).
- [15] S. Zhang, R. Liang, E. Zhang, L. Zhang, and Y. Liu, Phys. Rev. B **73**, 155316 (2006).
- [16] T. Stauber, N. M. R. Peres, and F. Guinea, Phys. Rev.

- B **76**, 205423 (2007); K. Nomura and A. H. MacDonald, Phys. Rev. Lett. **98**, 076602 (2007).
- [17] M. Tahir and P. Vasilopoulos, Phys. Rev. B **94**, 045415 (2016).
- [18] Z. Li and J. P. Carbotte, Phys. Rev. B **88**, 045414 (2013); E. Illes and E. J. Nicol, *ibid.* **94**, 125435 (2016).
- [19] P. Vasilopoulos and F.M. Peeters, Phys. Rev. B **40**, 10079 (1989).
- [20] V. Ryzhii, M Ryzhii, N. Ryabova, V. Mitin, and T. Otsuji, Jpn. J. Appl. Phys. **48**, 04C144 (2009).

